Coherent and incoherent spin-relaxation dynamics of electron-hole pairs in a π-conjugated polymer at low magnetic fields

T. H. Tennahewa,[1] S. Hosseinzadeh,[1] S. I. Atwood,[1] H. Popli,[1] H. Malissa,[1,2] J. M. Lupton,[1,2] and C. Boehme[1]

[1]*Department of Physics and Astronomy, University of Utah, Salt Lake City, Utah 84112, USA*

[2]*Institut für Experimentelle und Angewandte Physik, Universität Regensburg, Universitätsstrasse 31, 93053 Regensburg, Germany*

(Received 30 September 2022; revised 13 December 2023; accepted 14 December 2023; published 12 February 2024)

We report room-temperature measurements of the spin-relaxation times T_1 and T_2 of electron-hole charge-carrier spins in an organic light-emitting diode based on the π-conjugated polymer SY-PPV at low ($1\,\mathrm{mT} \lesssim B_0 \lesssim 10\,\mathrm{mT}$) static magnetic fields, using electrically detected—through spin-Rabi oscillation-controlled recombination currents—magnetic resonant Hahn-echo and inversion-recovery pulse sequences. When random local hyperfine fields and external magnetic fields compete in magnitude, charge carrier spin-quantization axes are no longer well defined, and striking magnetic-field dependencies of spin-lattice relaxation times are found, while spin coherence times remain mostly field-independent. These results corroborate the magnetic-field sensitivities of observables governed by radical-pair physics.

DOI: 10.1103/PhysRevB.109.075303

I. INTRODUCTION

The strong magnetic-field sensitivity of radical-pair systems has intrigued researchers for decades, from biologists studying avian magnetoreception [1,2] and chemists exploring magnetic-field-dependent reaction rates [3,4], to physicists investigating the pronounced low-field magnetoresistance of organic [5,6] and some disordered inorganic [7] semiconductors, where charge-carrier recombination currents follow the dynamics of the radical-pair process [8]. Common to all these systems is that they exhibit observables governed by nonequilibrium electronic relaxation processes that are subject to spin selection rules arising from inherently weak spin-orbit coupling [9]. It has been well established that the strong magnetic-field dependence of these processes is caused by a competition between externally applied magnetic fields and local internal hyperfine fields, which are distributed randomly in magnitude and direction [10]. When external fields become dominant over local hyperfine fields, the paramagnetic electronic states experience a change of their individual spin quantization axis, which, in turn, changes the permutation symmetry of the pair spin ensemble [11], causing variations of the spin-dependent transition rate, and thus, of observables such as the recombination current [12], light emission [13], or the perception of light by certain bird species [14]. While there is an abundance of data corroborating the magnetic-field dependence of observables governed by the radical-pair mechanism, there is still one key implication of this model that has not previously been scrutinized experimentally: the pronounced magnetic-field dependence of the longitudinal spin-relaxation time T_1. This dependence is predicted by the radical-pair model [2]. In addition, there may possibly also be a field dependence of the transverse spin-relaxation time T_2. Such dependencies of T_1 and T_2 should be pronounced within the range of applied magnetic fields in which the carrier pairs experience a change of the axis of quantization [5]. Since the direction of a general quantization axis becomes ill-defined for many spin pairs within this field range, the longitudinal and transverse directions also become ill-defined, along with the observables T_1 and T_2. The key challenge for an experimental test of this effect is to *measure* spin relaxation at vanishingly small magnetic field strengths.

Spin-relaxation times are most accurately determined using pulsed magnetic-resonance techniques [15]. However, these methods typically require sufficient spin polarization, and therefore, cannot be applied to the range of low magnetic fields of relevance here.

In this article, we present experimental evidence for significant variations in the spin-relaxation rate of a spin-pair system in the presence of an external magnetic field with a magnitude close to that arising from the random hyperfine fields. We overcome the above-mentioned experimental challenges by using pulsed electrically detected magnetic resonance (pEDMR) spectroscopy, exploiting the spin-dependent recombination currents in an organic light-emitting diode (OLED) of the commercial light-emitting conjugated polymer, Super-yellow-PPV (SY-PPV), a poly(phenylene-vinylene) copolymer (Sigma-Aldrich). These currents are governed by the spin dynamic processes of short-lived charge carrier pairs that are weakly spin-coupled (i.e., dipolar or exchange) in analogy to the presumptions laid out in the radical-pair mechanism [16] and thus allow the observation of magnetic resonance without the need of creating spin polarization.

The low-field magnetoconductance of a SY-PPV OLED (at a base current of $I \approx 20\,\mu\mathrm{A}$) is shown in Fig. 1(a). The curve exhibits the characteristic shape that has been observed in similar devices [17–19], as predicted for charge-carrier recombination processes that follow the spin statistics of radical pairs [10,20,21] at low magnetic fields. Figure 1(b) illustrates how the total static magnetic fields B_{Net} experienced by each charge carrier in the pair is made up of the vector sum of external field B_0 and local hyperfine field B_{hyp}. Since the spatial localization of molecular orbitals of both charge carriers

 ©2024 American Physical Society

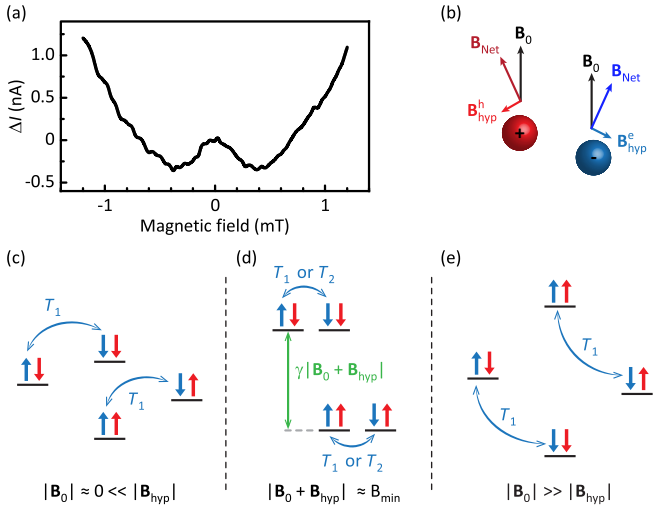

FIG. 1. (a) DC current change ΔI (magnetoconductance) of a SY-PPV OLED as a function of an external magnetic field strength of below ∼1.2 mT. The device has a 20 μA forward bias current. (b) Vector diagram of the total static magnetic fields of a charge-carrier pair. B_0 represents the external magnetic field, whereas B^{e}_{hyp} and B^{h}_{hyp} indicate the randomly oriented hyperfine magnetic fields experienced by electron and hole, respectively. B_{Net} is the vector sum of B_0 and the respective hyperfine fields. (c)–(e) Energy-level diagrams of two weakly spin-coupled charge-carrier pairs at (c) low applied magnetic field ($|B_0| \ll |B_{hyp}|$), (d) intermediate field ($|B_0 + B_{hyp}| \approx B_{min}$), and (e) high fields ($|B_0| \gg |B_{hyp}|$). Blue arrows indicate level transitions, i.e., spin-relaxation processes.

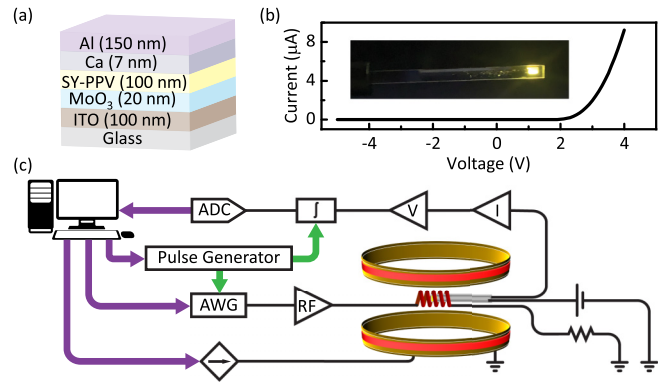

FIG. 2. (a) SY-PPV device structure used in this study. (b) I-V curve of a SY-PPV OLED at room temperature and a photograph of the OLED under bipolar charge-carrier injection. (c) Sketch of the experimental setup, consisting of (i) the circuit that applies a voltage bias to the OLED and converts the current change ΔI to a voltage signal, (ii) the RF circuit that generates and amplifies the RF pulses at the coil, including a 50 Ω power resistor for dissipation, and (iii) the circuit that controls the magnetic field. Black lines correspond to analog signal lines and green arrows correspond to TTL trigger signals that control the timing of the experiment. Purple arrows correspond to digital control and acquisition lines.

differs [22], the individual B_{hyp} vectors are randomly oriented in magnitude and direction. This difference leads to a distribution of the local magnetic fields and Zeeman energies, which inhibits degeneracy of the spin-pair states in the absence of an external field. As a field is applied, the spin-pair states shift in energy so that the Zeeman splitting either increases or decreases, depending on the mutual orientation of B_0 and B_{hyp}. Note that the relative offset of the spin-pair energies is very small—of order 100 neV—because of the very weak electronic dipole-dipole and exchange coupling, which was measured previously [23]. Figures 1(c) to 1(e) illustrate this process for increasing B_0. Figure 1(d) indicates a special case where the strength of B_0 is such that the levels with mixed S (singlet) and T_0 (superposition triplet) character are aligned with the pure triplet levels T_+ (↑↑) and T_- (↓↓), respectively. In this situation, spin-lattice relaxation processes, which usually involve energy exchange between the spin system and the lattice via phonons, become indistinguishable from mere decoherence processes, and the distinction between the spin-lattice relaxation time T_1 and the decoherence time T_2 is lost. As T_1 is typically larger than T_2, this indistinguishability implies that the difference between T_1 and T_2 must have a strong dependence on B_0 within this magnetic-field regime—a phenomenon that has yet to be established experimentally.

II. EXPERIMENTS

For pulsed EDMR experiments, well-established pulse sequences [24–28] for the determination of T_2 (i.e., electron spin-echo envelope modulation, ESEEM) and T_1 (i.e., inversion recovery) were adapted from conventional inductively detected EPR spectroscopy by the addition of readout pulses [28], with appropriate modification of the phase-cycling sequence [29]. While low-field continuous-wave EDMR experiments have previously been conducted on OLEDs [12,30–34], SiC MOSFETS [35], and Si:P structures [36], experiments that involve *pulsed* EDMR (pEDMR) at low excitation frequencies have only been demonstrated in the past in the context of spin-dependent processes in crystalline silicon systems [37,38]. Here, we report pEDMR on OLED recombination currents for extremely small frequencies of 40 MHz to 200 MHz, corresponding to resonance fields below 8 mT. Under these conditions, the effects of the random hyperfine fields on spin relaxation are expected to be most pronounced.

A. Sample preparation

The OLED samples used in this study were fabricated on glass substrates (SPI Supplies) with lithographically defined ITO contacts as described previously [18,25,39–41]. For hole injection, a 20-nm-thick layer of MoO_3 (Sigma-Aldrich) was spin-coated at 500 rpm for 3 s and at 2000 rpm for 20 s, followed by thermal annealing at 110 °C for 10 min [42]. SY-PPV [33,39,40] was dissolved in 1,2-dichlorobenzene at a concentration of 10 g/L, and then a 100-nm-thick layer of the solution was spin-coated inside a N_2 glovebox at 1000 rpm for 60 s, followed by thermal annealing at 110 °C for 10 min. Finally, 7 nm of calcium and then 150 nm of aluminum were thermally evaporated at a pressure of $<5 \times 10^{-6}$ mbar to form the electron injecting layer and the contact electrode. The device was encapsulated using Araldite 2011 epoxy. The device structure is shown in Fig. 2(a), and a picture of the OLED with its 2 mm × 3 mm pixel under operating conditions is shown in Fig. 2(b). The exponential I-V curve shown in Fig. 2(b),

measured using a Keithley 2450 source meter, confirms bipolar injection of electrons and holes.

B. Spectrometer setup

The pulsed EDMR setup is illustrated in Fig. 2(c) and consists of a homebuilt Helmholtz coil pair [34] driven by a computer-controlled current source (BK Precision 9202) that provides a static magnetic field B_0 of up to 15 mT, and a radio frequency (RF) coil (diameter 4 mm, length 4 mm, 4 loops, $L \approx 63$ nH) wrapped around the OLED to apply an oscillating field B_1 [34,43]. The RF pulses are directly synthesized by a computer-controlled arbitrary waveform generator (AWG, Wavepond Dax22000 with a sampling rate of 2.5 GHz) and amplified by two solid-state RF amplifiers (Mini-Circuits ZHL-100W-251-S+ with 46 dB gain in the frequency range 50 MHz to 250 MHz to and ENI 5100L with 50 dB gain for frequencies <50 MHz). The pulses are applied to the RF coil and dissipated at a 50 Ω power resistor. In addition, the pulses are monitored through the voltage drop across the resistor using a potentiometer network [not shown in Fig. 2(c)]. The OLED is powered by a low-noise voltage source (SRS SIM928) that is adjusted to apply a DC device current of approximately 20 μA, and the device current change is measured using a transimpedance amplifier (SRS SR570 with a gain of 2 μA/V) with a 10 Hz to 100 kHz band-pass filter. The resulting voltage signal is again amplified (SRS SR560 with a gain of 50 and a 100 kHz low-pass filter) and is either directly recorded by a computer-controlled digitizer (AlazarTech ATS 9462) or, in the case of charge measurements, integrated over an interval of 15 μs using a boxcar integrator (SRS SR250 with a gain of 5 mV/V and a 10 Hz high-pass filter) [25]. The resulting charge signal from the boxcar integrator is digitized by an analog-digital converter (ADC, National Instruments PCI 6251). The timing of the pulsed measurement is controlled through a pattern generator (Spincore Pulseblaster DDS-I-300) that triggers the AWG output and, depending on the type of measurement, either the digitizer or the boxcar integrator and the ADC acquisition. Computer control of the field generator, the AWG, the pattern generator, and the digitizer/ADC is established through custom-written software in MATLAB.

C. Pulse synthesis

Short rectangular RF pulses, as are required for coherent spin control [23,25–27,41,43], are challenging to produce. In conventional EPR spectrometers operating at microwave frequencies, this is achieved by pulse-forming units, which modulate a continuous-wave source with switches (e.g., PIN diodes) to form pulses of duration typically in the lower nanosecond range. At a much lower excitation frequency of ∼100 MHz, the pulse length is of the order of a single oscillation period, and the finite response time of the RF switches may significantly distort the pulse shape. Longer, lower-power RF pulses are not desirable due to their reduced excitation bandwidth with respect to the inhomogeneously broadened resonance spectrum of the spin ensemble. In addition, such long so-called soft pulses would require pulse sequences exceeding the charge-carrier spin coherence times. We therefore synthesized RF pulses directly using an arbitrary waveform generator (AWG) and confirmed the excitation profile by calculating the Fourier transform of the pulse waveform. The excitation profile follows a sinc function (centered around the excitation frequency with a width that is inversely proportional to the pulse duration), which is characteristic of a rectangular pulse even for pulse lengths that are substantially lower than the oscillation period [44]. For multipulse sequences, the phases of the pulses are adjusted such that the oscillation is coherent throughout the entire sequence.

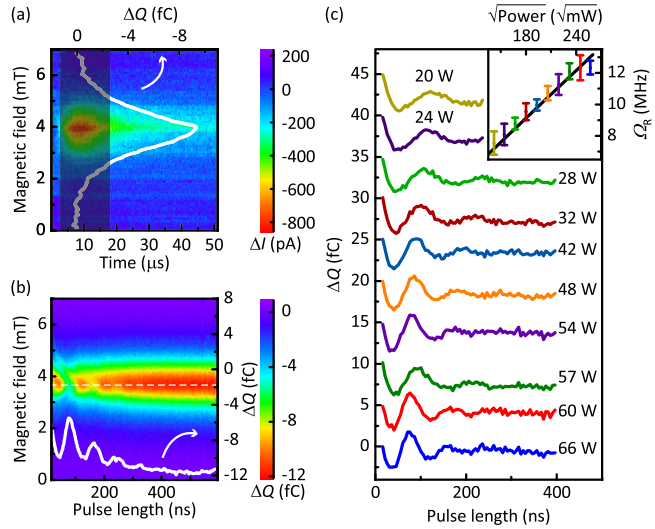

FIG. 3. (a) Relative changes in current ΔI following a short RF pulse of duration 100 ns and frequency of 100 MHz as a function of time after the pulse and external magnetic field strength B_0. The white trace corresponds to the integrated current change ΔQ, integrated over a 15 μs interval (shaded region) using a boxcar integrator. (b) ΔQ as a function of RF pulse length and magnetic field. The white line indicates ΔQ as a function of pulse length at the resonance maximum at $B_0 = 3.77$ mT (indicated by the dashed line), clearly showing Rabi oscillations. (c) ΔQ as a function of pulse length at the resonance maximum for different RF powers. The inset shows the Rabi frequency Ω_R, determined by Fourier transformation, as a function of power. The black line corresponds to a numerical least-squares fit of $\Omega_R \propto \sqrt{\text{Power}}$.

III. RESULTS

A. Spectra and transient nutations

Figure 3(a) shows the pEDMR signal following a 100-ns-long 100-MHz RF pulse (RF power of 66 W) as a function of magnetic field as it is swept through resonance. These measurements, as all measurements presented in this article, were conducted at room temperature. The heatmap corresponds to the digitized transients of the OLED current change following the pulse, measured by sweeping the static magnetic field B_0 four times, whereas the solid white line represents the boxcar-integrated signal measured in a separate single-scan experiment. The shaded region indicates the integration interval. A sharp resonance is visible at $B_0 = 3.77$ mT, which corresponds to the $g \approx 2.00$ resonance in SY-PPV [33,39,40]. The transient measurement has a single-scan signal-to-noise

ratio (SNR) of 10, whereas the single-scan SNR of the integrated measurement is 22. In the following, we will only consider the boxcar-integrated measurements because of the greater sensitivity and the fact that the information contained in the temporal dynamics of the current response following RF excitation is not relevant for the presented work.

To demonstrate coherent RF control, we perform transient nutation measurements, i.e., measurements of the integrated current change following a 100 MHz RF pulse of varying duration [23,41,43] as a function of magnetic field swept across the resonance at $B_0 = 3.77$ mT. Results are shown in Fig. 3(b): the heatmap displays ΔQ as a function of pulse duration and magnetic field (bottom and left-hand axes), whereas the solid white line shows ΔQ (right-hand axis) as a function of pulse length for $B_0 = 3.77$ mT. The dashed, horizontal white line marks the on-resonance slice of the data shown by the solid white line. The on-resonance ΔQ shows several periods of oscillation, which quickly disappear when the field moves off-resonance (not shown). To confirm that these oscillations indeed arise due to spin Rabi flopping [41], we performed this measurement at different RF powers between 20 W and 66 W, as shown in Fig. 3(c). The oscillation frequency Ω_R indeed scales with the strength of B_1, which is proportional to the square root of the RF power, as shown in the inset of Fig. 3(c).

B. Spin relaxation times

To assess the spin-relaxation times T_1 and T_2 in the low-field regime, we applied Hahn-echo [25–29] and inversion-recovery [24,27] pulse sequences as indicated in Figs. 4(a) and 4(d). These sequences correspond to conventional EPR Hahn-echo [27,28,45] and inversion-recovery measurements [24,27], with an additional $\pi/2$ readout pulse applied at the timing of the echo maximum. This additional pulse rotates the spins onto the axis of quantization to allow the charge signal ΔQ to be determined, i.e., it constitutes a readout pulse [46]. Nonresonant spin-independent signal contributions as well as additional echoes are removed by phase cycling, with four steps for the Hahn echo and eight steps for inversion recovery [25,29]. For each measurement, the pulse sequences depicted in Figs. 4(a) and 4(d) were repeated 2000 times at a shot repetition rate of 500 Hz. In Fig. 4(b), the Hahn echo at $\nu = 100$ MHz, i.e., at resonance, is shown. For this measurement, the time interval τ' [as defined in Fig. 4(a)] is varied, while τ is kept fixed at 400 ns. The duration of the π-pulse is kept constant at 62 ns for all measurements, and the requisite RF power is determined by measuring the Rabi oscillations using Hahn-echo detection and adjusting the RF power to produce π-rotations. The delay between the readout-pulse and the start of the integration window is kept constant at 1500 ns, which yields the maximum single-shot SNR of 2.8. The baseline before and after the leading and trailing edge of the echo is distributed around zero, indicating complete cancellation of the nonresonant background signal by the correct choice of phase settings. Figure 4(c) shows the Hahn-echo amplitude as a function of τ from 88 ns to 1000 ns for $\tau = \tau'$, i.e., detected at the echo maximum, with all other parameters identical to Fig. 4(b). These settings constitute an electrically detected electron spin-echo envelope modulation (ESEEM)

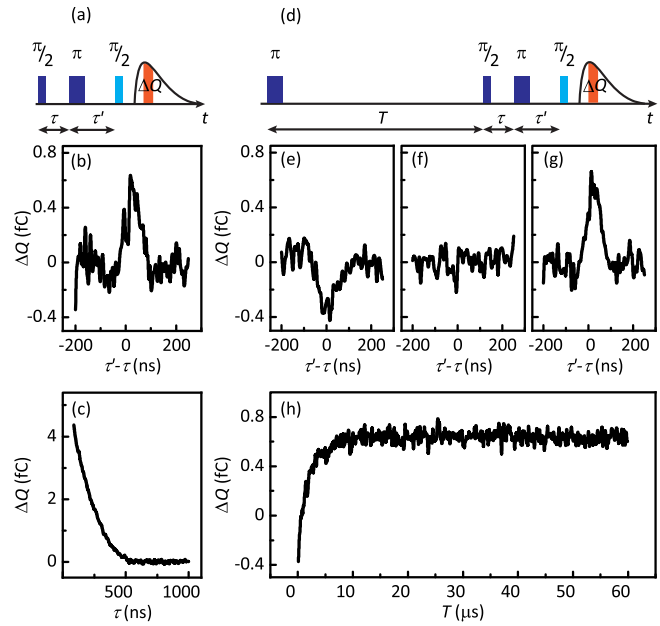

FIG. 4. (a) Pulse sequence for electrically detected Hahn echoes and ESEEM. (b) ΔQ as a function of τ' with $\tau = 400$ ns and an excitation frequency of 100 MHz, using a four-step phase-cycling sequence as described in Refs. [25,29] (i.e., an electrically detected Hahn echo). (c) ΔQ as a function of $\tau = \tau'$ (i.e., electrically detected ESEEM). (d) Pulse sequence for electrically detected inversion recovery. (e)–(g) ΔQ as a function of τ' with $\tau = 400$ ns and (e) $T = 200$ ns, (f) $T = 800$ ns, and (g) $T = 50$ μs, using an eight-step phase-cycling sequence (i.e., an electrically detected inversion echo). (h) ΔQ as a function of T for $\tau = \tau' = 400$ ns (i.e., electrically detected inversion recovery).

measurement. The electrically detected echo envelope follows a stretched exponential decay with a time constant of T_2. In Fig. 4(c), we obtain $T_2 = (469 \pm 7)$ ns, which is comparable to the value previously obtained at much higher fields and frequencies (345 mT, 10 GHz) [24].

Next, we consider inversion-recovery echoes in Figs. 4(e)–4(g) as a function of τ', with $\tau = 400$ ns and $T = 200$ ns, 800 ns, and 50 μs [as defined in Fig. 4(d)], respectively. These settings correspond to the inverted echo, the echo that changes sign from negative to positive, and the fully recovered echo, respectively. The progression of the echoes with delay time reflects the exponential dependence of ΔQ on T with the characteristic time constant T_1, as seen in Fig. 4(h). At 100 MHz, we obtain $T_1 = (1.8 \pm 0.1)$ μs, which is considerably *shorter* than the value of T_1 previously determined for SY-PPV at X-band (10 GHz) [24] and for similar conjugated-polymer materials [26,47].

IV. DISCUSSION

Finally, we explore the dependence of spin-relaxation times T_1 and T_2 on the excitation frequency below 200 MHz. Figure 5(a) plots the integrated current response following a single excitation pulse (200 ns duration) as a function of magnetic field and excitation frequency. To find the resonance centers, spectra were fitted with a combination of a

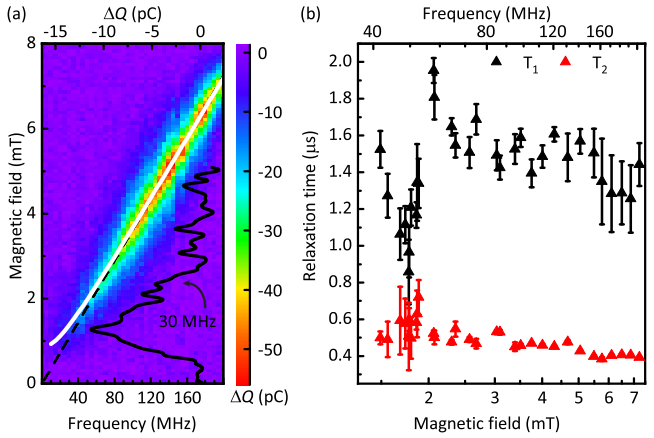

FIG. 5. (a) Integrated current change ΔQ following a 200 ns RF pulse as a function of excitation frequency and magnetic field. The white line shows a fit of the resonance maximum to the expected net field strength experienced by the spins, B_{Net}. The solid black line shows ΔQ (top horizontal axis) as a function of magnetic field at 30 MHz. The dashed line indicates Zeeman resonances following the canonical relation $h\nu = g\mu_B B_0$. (b) Linear-log plot of spin-relaxation times as a function of the resonance field and frequency. Each data point represents the weighted average of several measurements under nominally identical conditions, as described in the Supplemental Material [44].

double Gaussian function and a first-order polynomial, which takes the magnetoresistance effects into consideration. Above 40 MHz, the dependence of the resonance frequency on field strength is trivial and follows $g\mu_B B_0 = h\nu$, as indicated by the black dashed line. However, at excitation frequencies below 30 MHz, the resonance peak starts to deviate, as indicated by the solid white line, which is the result of a fit function that depends on the hyperfine field and the net magnetic field experienced by the spins fitted to the experimentally determined resonance maxima. This deviation from the linear relationship is caused by the competition of the externally applied magnetic field and the random hyperfine fields B_{hyp}, which are comparable in magnitude. The experimentally determined resonance centers were fitted with $B_{\mathrm{Net}} = \sqrt{B_{\mathrm{hyp}}^2 + (\frac{h\nu}{g\mu_B})^2}$, which takes this competition into account [cf. the white line in Fig. 5(a)]. The resulting value of $B_{\mathrm{hyp}} = 0.9$ mT is comparable to previously obtained results [39]. In addition, under conventional EPR conditions, only one helicity component of the linearly polarized amplitude B_1 of the oscillating magnetic field is active. However, as B_1 approaches and exceeds B_0, both helicities become EPR active, giving rise to the Bloch-Siegert shift of the resonance [31]. A complete set of spectra is shown in the Supplemental Material [44].

Figure 5(b) plots the T_1 and T_2 values extracted from the electrically detected inversion recovery and ESEEM measurements as discussed in Fig. 4, performed at different RF frequencies. The values are plotted as a function of the resonance field, and the error bars indicate the uncertainty arising from a numerical least-squares fit of the resonance spectra. The values for T_2 appear quite constant and scatter around $T_2 = (495 \pm 77)$ ns (i.e., within the error bars), which is consistent with the T_2 value previously determined at X-band frequencies [24]. In contrast, the T_1 values exhibit a striking magnetic-field dependence: at frequencies above 60 MHz, T_1 appears constant at (1.5 ± 0.1) μs, whereas at lower frequencies, it decreases steeply to (0.9 ± 0.2) μs at 44 MHz. Remarkably, for the lowest frequencies, T_1 rises again to (1.5 ± 0.1) μs. This distinct and nonmonotonic behavior is consistent with the radical-pair model of magnetic-field effects in molecular systems as illustrated in Figs. 1(c) to 1(e); in the intermediate-strength field regime [cf. Fig. 1(d)], the mixed singlet (S) and pure triplet (T_0) levels of the spin pair become energetically aligned with T_+ and T_-, respectively. Under this condition, spin-lattice relaxation processes become indistinguishable from spin-spin relaxation processes. This indistinguishability is reflected by the results in Fig. 5(b), which indicate that $T_1 \approx T_2 = (0.9 \pm 0.2)$ μs in the ultralow field regime, whereas $T_1 > T_2$ for higher and lower magnetic fields, where this level alignment no longer occurs and T_1 processes require a phonon to exchange energy with the environment. This observation is qualitatively consistent with the ultrasmall magnetic-field effect that is observed, e.g., in magnetoresistance and magnetoelectroluminescence of OLEDs [19], but also in magnetic-field effects in chemical reactions in solution detected by photoinduced absorption [48].

V. CONCLUSIONS

We demonstrated low-field *coherent* spin control in OLEDs at room temperature in a low-frequency pEDMR spectrometer employing direct RF-pulse synthesis. Both coherent and incoherent spin-relaxation times are measured as a function of resonance frequency in the range from 40 MHz to 200 MHz by electrically detected ESEEM and inversion-recovery. Our results indicate that T_2 remains relatively constant over the frequency range in question and is comparable to values reported previously for much higher excitation frequencies [24], whereas T_1, which exceeds T_2 for most frequencies, shows a striking quenching at around 44 MHz, below which it becomes comparable in magnitude to T_2. We attribute this dependency to a shift of the energy levels of the charge-carrier spin-pair states due to the random hyperfine fields experienced by each pair partner. These hyperfine fields become comparable to the external magnetic field at low frequencies and lead to the ultrasmall magnetic-field effect in observables that depend on the radical-pair mechanism, including magnetoconductance in OLEDs [19].

ACKNOWLEDGMENTS

This work has been supported the U.S. Department of Energy, Office of Basic Energy Sciences, Division of Materials Sciences and Engineering under Award No. DE-SC0000909. H. M. acknowledges support from the Deutsche Forschungsgemeinschaft (DFG, German Research Foundation) (project ID 314695032–SFB 1277, subproject No. B03).

[1] C. T. Rodgers and P. J. Hore, Chemical magnetoreception in birds: The radical pair mechanism, Proc. Natl. Acad. Sci. USA **106**, 353 (2009).

[2] T. Ritz, S. Adem, and K. Schulten, A model for photoreceptor-based magnetoreception in birds, Biophys. J. **78**, 707 (2000).

[3] C. T. Rodgers, Magnetic field effects in chemical systems, Pure Appl. Chem. **81**, 19 (2009).

[4] C. B. Vink and J. R. Woodward, Effect of a weak magnetic field on the reaction between neutral free radicals in isotropic solution, J. Am. Chem. Soc. **126**, 16730 (2004).

[5] T. D. Nguyen, G. Hukic-Markosian, F. Wang, L. Wojcik, X.-G. Li, E. Ehrenfreund, and Z. V. Vardeny, Isotope effect in spin response of π-conjugated polymer films and devices, Nat. Mater. **9**, 345 (2010).

[6] S. P. Kersten, A. J. Schellekens, B. Koopmans, and P. A. Bobbert, Magnetic-field dependence of the electroluminescence of organic light-emitting diodes: A competition between exciton formation and spin mixing, Phys. Rev. Lett. **106**, 197402 (2011).

[7] M. J. Mutch, P. M. Lenahan, and S. W. King, Spin transport, magnetoresistance, and electrically detected magnetic resonance in amorphous hydrogenated silicon nitride, Appl. Phys. Lett. **109**, 062403 (2016).

[8] H. Kraus, S. Bange, F. Frunder, U. Scherf, C. Boehme, and J. M. Lupton, Visualizing the radical-pair mechanism of molecular magnetic field effects by magnetic resonance induced electrofluorescence to electrophosphorescence interconversion, Phys. Rev. B **95**, 241201(R) (2017).

[9] E. L. Frankevich, A. A. Lymarev, I. Sokolik, F. E. Karasz, S. Blumstengel, R. H. Baughman, and H. H. Hörhold, Polaron-pair generation in poly(phenylene vinylenes), Phys. Rev. B **46**, 9320 (1992).

[10] W. Wagemans, P. Janssen, A. J. Schellekens, F. L. Bloom, P. A. Bobbert, and B. Koopmans, The many faces of organic magnetoresistance, SPIN **01**, 93 (2011).

[11] R. Haberkorn and W. Dietz, Theory of spin-dependent recombination in semiconductors, Solid State Commun. **35**, 505 (1980).

[12] W. J. Baker, K. Ambal, D. P. Waters, R. Baarda, H. Morishita, K. van Schooten, D. R. McCamey, J. M. Lupton, and C. Boehme, Robust absolute magnetometry with organic thin-film devices, Nat. Commun. **3**, 898 (2012).

[13] C. G. Yang, E. Ehrenfreund, and Z. V. Vardeny, Polaron spin-lattice relaxation time in π-conjugated polymers from optically detected magnetic resonance, Phys. Rev. Lett. **99**, 157401 (2007).

[14] R. Wiltschko, K. Stapput, P. Thalau, and W. Wiltschko, Directional orientation of birds by the magnetic field under different light conditions, J. R. Soc. Interface. **7**, S163 (2010).

[15] A. Schweiger and G. Jeschke, *Principles of Pulse Electron Paramagnetic Resonance* (Oxford University Press, Oxford, 2001).

[16] D. R. McCamey, K. J. van Schooten, W. J. Baker, S.-Y. Lee, S.-Y. Paik, J. M. Lupton, and C. Boehme, Hyperfine-field-mediated spin beating in electrostatically bound charge carrier pairs, Phys. Rev. Lett. **104**, 017601 (2010).

[17] G. Joshi, M. Y. Teferi, R. Miller, S. Jamali, M. Groesbeck, J. van Tol, R. McLaughlin, Z. V. Vardeny, J. M. Lupton, H. Malissa, and C. Boehme, High-field magnetoresistance of organic semiconductors, Phys. Rev. Appl. **10**, 024008 (2018).

[18] A. H. Devir-Wolfman, B. Khachatryan, B. R. Gautam, L. Tzabary, A. Keren, N. Tessler, Z. V. Vardeny, and E. Ehrenfreund, Short-lived charge-transfer excitons in organic photovoltaic cells studied by high-field magneto-photocurrent, Nat. Commun. **5**, 4529 (2014).

[19] E. Ehrenfreund and Z. V. Vardeny, Effects of magnetic field on conductance and electroluminescence in organic devices, Isr. J. Chem. **52**, 552 (2012).

[20] Y. Sheng, T. D. Nguyen, G. Veeraraghavan, Ö. Mermer, and M. Wohlgenannt, Effect of spin-orbit coupling on magnetoresistance in organic semiconductors, Phys. Rev. B **75**, 035202 (2007).

[21] P. Janssen, M. Cox, S. H. W. Wouters, M. Kemerink, M. M. Wienk, and B. Koopmans, Tuning organic magnetoresistance in polymer-fullerene blends by controlling spin reaction pathways, Nat. Commun. **4**, 2286 (2013).

[22] H. Malissa, R. Miller, D. L. Baird, S. Jamali, G. Joshi, M. Bursch, S. Grimme, J. van Tol, J. M. Lupton, and C. Boehme, Revealing weak spin-orbit coupling effects on charge carriers in a π-conjugated polymer, Phys. Rev. B **97**, 161201(R) (2018).

[23] K. J. van Schooten, D. L. Baird, M. E. Limes, J. M. Lupton, and C. Boehme, Probing long-range carrier-pair spin-spin interactions in a conjugated polymer by detuning of electrically detected spin beating, Nat. Commun. **6**, 6688 (2015).

[24] M. Groesbeck, H. Liu, M. Kavand, E. Lafalce, J. Wang, X. Pan, T. H. Tennahewa, H. Popli, H. Malissa, C. Boehme, and Z. V. Vardeny, Separation of spin and charge transport in pristine π-conjugated polymers, Phys. Rev. Lett. **124**, 067702 (2020).

[25] H. Malissa, M. Kavand, D. P. Waters, K. J. van Schooten, P. L. Burn, Z. V. Vardeny, B. Saam, J. M. Lupton, and C. Boehme, Room-temperature coupling between electrical current and nuclear spins in OLEDs, Science **345**, 1487 (2014).

[26] W. J. Baker, T. L. Keevers, J. M. Lupton, D. R. McCamey, and C. Boehme, Slow hopping and spin dephasing of coulombically bound polaron pairs in an organic semiconductor at room temperature, Phys. Rev. Lett. **108**, 267601 (2012).

[27] S.-Y. Paik, S.-Y. Lee, W. J. Baker, D. R. McCamey, and C. Boehme, T_1 and T_2 spin relaxation time limitations of phosphorous donor electrons near crystalline silicon to silicon dioxide interface defects, Phys. Rev. B **81**, 075214 (2010).

[28] H. Huebl, F. Hoehne, B. Grolik, A. R. Stegner, M. Stutzmann, and M. S. Brandt, Spin echoes in the charge transport through phosphorus donors in silicon, Phys. Rev. Lett. **100**, 177602 (2008).

[29] F. Hoehne, L. Dreher, M. Suckert, D. P. Franke, M. Stutzmann, and M. S. Brandt, Time constants of spin-dependent recombination processes, Phys. Rev. B **88**, 155301 (2013).

[30] T. Grünbaum, S. Bange, W. Jiang, A. E. Leung, T. A. Darwish, P. L. Burn, and J. M. Lupton, Measuring the magnetic field amplitude of rf radiation by the quasistatic magnetic field effect in organic light-emitting diodes, Phys. Rev. Appl. **15**, 064001 (2021).

[31] S. Jamali, V. V. Mkhitaryan, H. Malissa, A. Nahlawi, H. Popli, T. Grünbaum, S. Bange, S. Milster, D. M. Stoltzfus, A. E. Leung, T. A. Darwish, P. L. Burn, J. M. Lupton, and C. Boehme, Floquet spin states in OLEDs, Nat. Commun. **12**, 465 (2021).

[32] T. Grünbaum, S. Milster, H. Kraus, W. Ratzke, S. Kurrmann, V. Zeller, S. Bange, C. Boehme, and J. M. Lupton, OLEDs as models for bird magnetoception: detecting electron spin resonance in geomagnetic fields, Faraday Discuss. **221**, 92 (2020).

[33] S. Jamali, G. Joshi, H. Malissa, J. M. Lupton, and C. Boehme, Monolithic OLED-microwire devices for ultrastrong magnetic resonant excitation, Nano Lett. **17**, 4648 (2017).

[34] D. P. Waters, G. Joshi, M. Kavand, M. E. Limes, H. Malissa, P. L. Burn, J. M. Lupton, and C. Boehme, The spin-dicke effect in OLED magnetoresistance, Nat. Phys. **11**, 910 (2015).

[35] J. P. Ashton, B. R. Manning, S. J. Moxim, F. V. Sharov, P. M. Lenahan, and J. T. Ryan, Intermediate spin pair relaxation through modulation of isotropic hyperfine interaction in frequency-swept spin-dependent recombination in 4H-SiC, Appl. Phys. Lett. **120**, 062403 (2022).

[36] H. Morishita, L. S. Vlasenko, H. Tanaka, K. Semba, K. Sawano, Y. Shiraki, M. Eto, and K. M. Itoh, Electrical detection and magnetic-field control of spin states in phosphorus-doped silicon, Phys. Rev. B **80**, 205206 (2009).

[37] L. Dreher, F. Hoehne, H. Morishita, H. Huebl, M. Stutzmann, K. M. Itoh, and M. S. Brandt, Pulsed low-field electrically detected magnetic resonance, Phys. Rev. B **91**, 075314 (2015).

[38] F. M. Hrubesch, G. Braunbeck, A. Voss, M. Stutzmann, and M. S. Brandt, Broadband electrically detected magnetic resonance using adiabatic pulses, J. Magn. Reson. **254**, 62 (2015).

[39] G. Joshi, M. Y. Teferi, R. Miller, S. Jamali, D. Baird, J. van Tol, H. Malissa, J. M. Lupton, and C. Boehme, Isotropic effective spin-orbit coupling in a conjugated polymer, J. Am. Chem. Soc. **140**, 6758 (2018).

[40] M. Kavand, D. Baird, K. van Schooten, H. Malissa, J. M. Lupton, and C. Boehme, Discrimination between spin-dependent charge transport and spin-dependent recombination in π-conjugated polymers by correlated current and electroluminescence-detected magnetic resonance, Phys. Rev. B **94**, 075209 (2016).

[41] D. R. McCamey, H. A. Seipel, S.-Y. Paik, M. J. Walter, N. J. Borys, J. M. Lupton, and C. Boehme, Spin rabi flopping in the photocurrent of a polymer light-emitting diode, Nat. Mater. **7**, 723 (2008).

[42] J. Peng, X. Xu, C. Yao, and L. Li, Bi-layer hole-injecting layer composed of molybdenum oxide and polyelectrolyte for solution-processed OLEDs with prolonged stability, RSC Adv. **6**, 100312 (2016).

[43] D. M. Stoltzfus, G. Joshi, H. Popli, S. Jamali, M. Kavand, S. Milster, T. Grünbaum, S. Bange, A. Nahlawi, M. Y. Teferi, S. I. Atwood, A. E. Leung, T. A. Darwish, H. Malissa, P. L. Burn, J. M. Lupton, and C. Boehme, Perdeuteration of poly[2-methoxy-5-(2'-ethylhexyloxy)-1,4-phenylenevinylene] (d-MEH-PPV): control of microscopic charge-carrier spin-spin coupling and of magnetic-field effects in optoelectronic devices, J. Mater. Chem. C **8**, 2764 (2020).

[44] See Supplemental Material at http://link.aps.org/supplemental/10.1103/PhysRevB.109.075303 for details of pulse synthesis, and hardware and software control.

[45] J. Lu, F. Hoehne, A. R. Stegner, L. Dreher, M. Stutzmann, M. S. Brandt, and H. Huebl, High-resolution electrical detection of free induction decay and hahn echoes in phosphorus-doped silicon, Phys. Rev. B **83**, 235201 (2011).

[46] L. Childress, M. V. Gurudev Dutt, J. M. Taylor, A. S. Zibrov, F. Jelezko, J. Wrachtrup, P. R. Hemmer, and M. D. Lukin, Coherent dynamics of coupled electron and nuclear spin qubits in diamond, Science **314**, 281 (2006).

[47] D. R. McCamey, S.-Y. Lee, S.-Y. Paik, J. M. Lupton, and C. Boehme, Spin-dependent dynamics of polaron pairs in organic semiconductors, Phys. Rev. B **82**, 125206 (2010).

[48] C. Kerpal, S. Richert, J. G. Storey, S. Pillai, P. A. Liddell, D. Gust, S. R. Mackenzie, P. J. Hore, and C. R. Timmel, Chemical compass behaviour at microtesla magnetic fields strengthens the radical pair hypothesis of avian magnetoreception, Nat. Commun. **10**, 3707 (2019).